

Asteroid Impact Tsunami: A Probabilistic Hazard Assessment

Steven N. Ward and Erik Asphaug

Institute of Tectonics, University of California, Santa Cruz, CA 95064, USA.
ward@uplift.ucsc.edu; asphaug@cosmic.ucsc.edu

SUMMARY

We investigate the generation, propagation, and probabilistic hazard of tsunami spawned by oceanic asteroid impacts. The process first links the depth and diameter of parabolic impact cavities to asteroid density, radius, and impact velocity by means of elementary energy arguments and crater scaling rules. Then, linear tsunami theory illustrates how these transient cavities evolve into vertical sea surface waveforms at distant positions and times. By measuring maximum wave amplitude at many distances for a variety of impactor sizes, we derive simplified attenuation relations that account both for geometrical spreading and frequency dispersion of tsunami on uniform depth oceans. In general, the tsunami wavelengths contributing to the peak amplitude coincide closely with the diameter of the transient impact cavity. For the moderate size impactors of interest here (those smaller than a few hundred meters radius), cavity widths are less than or comparable to mid-ocean depths. As a consequence, dispersion increases the $1/\sqrt{r}$ long-wave decay rate to nearly $1/r$ for tsunami from these sources. In the final step, linear shoaling theory applied at the frequency associated with peak tsunami amplitude corrects for amplifications as the waves near land. By coupling this tsunami amplitude/distance information with the statistics of asteroid falls, the probabilistic hazard of impact tsunami is assessed in much the same way as probabilistic seismic hazard, by integrating contributions over all admissible impactor sizes and impact locations. In particular, tsunami hazard, expressed as the Poissonian probability of being inundated by waves from 2 to 50 meter height in a 1000 year interval, is computed at both generic (generalized geography) and specific (real geography) sites. For example, a typical generic site with 180 degrees of ocean exposure and a reach of 6,000 km, admits a 1-in-14 chance of an impact tsunami exceeding 2 meter height in 1000 years. The likelihood drops to 1-in-35 for a 5 meter wave, and to 1-in-345 for a 25 meter wave. Specific sites of Tokyo and New York have 1-in-24 and 1-in-47 chances of suffering an impact tsunami greater than 5 m in the next millennium.

Key words: Impact Processes, Cratering, Asteroids, Planetary Surfaces

1 INTRODUCTION

As do many natural disasters, impacts by asteroids pose less of a threat directly than they do by consequential events. The number of Earth's inhabitants that might be touched directly by asteroid explosion and cratering, pales to those potentially affected indirectly by obscuration of sunlight, global wildfires, polluting sedimentation, and noxious loading of the atmosphere (see *Toon et al.* 1995). Because two-thirds of the objects that strike Earth impact in water, yet another consequential threat that can be transmitted great distances are tsunami spawned by the collapse of pelagic impact cavities (*Gault and Sonnett* 1982; *Roddy et al.* 1987; *Hills et al.* 1994; *Nemtchinov et al.* 1996; *Crawford and Mader* 1998). As we shall see, impact tsunami hazard can reach perceptible levels on historical, even

human, time scales.

The Earth carries clear evidence of oceanic impact of asteroids and impact tsunami. *Gersonde et al.* (1997) document the collision of a 1 km or larger diameter asteroid into the Southern Ocean during the late Pliocene (2.15 Ma). Besides abundant fragments of the meteorite itself, sediment cores and echo soundings reveal tsunami-induced damage over hundreds of square kilometers of seafloor in the form of turbulent disturbances, eroded seamounts and buried ejecta. A more catastrophic incident, the K/T impact that ended the Cretaceous era of life 65 million years ago, spawned enormous waves when a ~10 km asteroid or comet struck a shallow sea presently near Chicxulub, Mexico. Tsunami from this impact deposited material widely and often far inland (e.g. *Smit et al.* 1996).

Recognition of tsunami deposits in Haiti, Texas, and Florida helped confirm the nature and location of the impact extinction event first proposed by *Alvarez et al.* (1980).

Mercifully, disasters of the magnitude of the K/T impact that leave permanent marks on the geological and biological record occur very infrequently. Accordingly, it might be more productive to turn attention from extinction-level impactors to ones of moderate scale – 30 to 500 m radius. Meteors of this size are thought to strike Earth’s oceans every 1,000 to 100,000 years. Moderate size impactors pose limited threat of catastrophe; still, because lesser size bodies have a high rate of fall, their tsunami may produce greater hazard within historical contexts than do tsunami spawned by much larger impactors. To develop a rigorous probabilistic assessment of tsunami hazard posed by moderate size asteroids, this paper couples statistics of asteroid impacts, idealizations of oceanic cavity formation, and linear theories of tsunami propagation and shoaling. Hazard, expressed as the probability of being inundated by waves from 2 to 50 meter height in a 1000 year interval, is computed at both generic (generalized geography) and specific (real geography) sites.

Clearly, success in this endeavor hinges on viable estimates of the flux of moderate size impactors into the Earth’s oceans. Unfortunately, astronomical censuses of moderate size objects that populate near Earth orbits are notoriously poor. Heavy and uncertain filtration by the atmosphere further blurs counts of those objects that survive to reach the Earth’s surface. Scientists know modern-era impact flux of 30 to 500 m size asteroids and comets perhaps to a factor of three at best. Given this ignorance, our hazard computations must make several assumptions including an impactor flux with a power law dependence on asteroid radius, and a high pass filter representation of atmospheric ablation. Nevertheless, because the underlying calculations for the total hazard can account for uncertainties in shoaling and impactor properties, can be “broken down” to assess the importance of impactor size distribution and impact location, can be set to variable levels of risk tolerance, and can be made geographically correct, our assessments improve current practice and break trail for future analyses.

2 IMPACT TSUNAMI THEORY

Tsunami Waveforms.

Under typical assumptions (inviscid and incompressible water, small material strain, irrotational motion, rigid seafloor), an instantaneously-formed ocean impact cavity of shape $u_z^{\text{impact}}(\mathbf{r}_0)$ produces vertical component tsunami waveforms at surface position \mathbf{r} and time t of

$$u_z^{\text{surf}}(\mathbf{r},t) = \frac{\text{Re}}{4\pi^2} \int_{\mathbf{k}} d\mathbf{k} e^{i(\mathbf{k}\cdot\mathbf{r}-\omega(k)t)} \int_{\mathbf{r}_0} d\mathbf{r}_0 u_z^{\text{impact}}(\mathbf{r}_0) e^{-i\mathbf{k}\cdot\mathbf{r}_0} \quad (1a)$$

with $r=|\mathbf{r}|$, $k=|\mathbf{k}|$, $\omega(k)=kc(k)=kv_t[\tanh(kh)/kh]^{1/2}$, $v_t=(gh)^{1/2}$, and h is a uniform ocean depth (*Ben-Menahem and Singh, 1981; Dingemans, 1997*). In this formula: Re means the real part; \mathbf{k} is a wavenumber; $c(k)$ is tsunami phase velocity; and $\omega(k)$ is the frequency associated with a given k . The integrals in (1a) cover all wavenumber space and locations \mathbf{r}_0 where $u_z^{\text{impact}}(\mathbf{r}_0) \neq 0$. The identities

$$\frac{1}{2\pi} \int_0^{2\pi} d\theta e^{i\mathbf{k}\cdot(\mathbf{r}-\mathbf{r}_0)} = J_0(kR) = \int_{n=-\infty}^{\infty} J_n(kr)J_n(kr_0)e^{in(\theta-\theta_0)}$$

transform (1a) to

$$u_z^{\text{surf}}(\mathbf{r},t) = \frac{\text{Re}}{2\pi} \int_0^\infty k dk e^{-i\omega(k)t} \int_{\mathbf{r}_0} d\mathbf{r}_0 u_z^{\text{impact}}(\mathbf{r}_0) J_0(kR) \quad (1b)$$

or

$$u_z^{\text{surf}}(\mathbf{r},t) = \frac{\text{Re}}{2\pi} \int_{n=-\infty}^{\infty} \int_0^\infty k dk J_n(kr) e^{-i(\omega(k)t-n\theta)} \int_{\mathbf{r}_0} d\mathbf{r}_0 u_z^{\text{impact}}(\mathbf{r}_0) J_n(kr_0) e^{-in\theta_0} \quad (1c)$$

where $R=|\mathbf{r}-\mathbf{r}_0|$ and the $J_n(x)$ are cylindrical Bessel functions. If $u_z^{\text{impact}}(\mathbf{r}_0)$ has a small number of azimuthal orders n , then (1c) is most convenient to program.

Initial Cavity Shape Generalities.

Suppose that the initial stage of cratering by moderate size impactors excavates a radially symmetric, parabolic cavity of depth D_c and inner and outer radii R_c and R_D

$$u_z^{\text{impact}}(\mathbf{r}) = D_C(1 - r^2/R_C^2) \quad r \leq R_D \quad (2)$$

$$u_z^{\text{impact}}(\mathbf{r}) = 0 \quad r > R_D$$

If $R_D=R_C$, all of the water within the cavity ejects incoherently into space and does not contribute to the tsunami. If $R_D=\sqrt{2}R_C$, all of the water within the cavity deposits coherently into a bordering lip and does contribute to the tsunami. The top row of Figure 1 illustrates the cavity shapes for these two cases. Transient initial cavity (2) evolves to propagating tsunami waves from (1c)

$$u_z^{\text{surf}}(\mathbf{r},t) = \int_0^{\infty} \frac{k \, dk}{2\pi} F(k,R_C,R_D) J_0(kr) \cos(\omega(k)t) \quad (3)$$

where

$$\begin{aligned} F(k,R_C,R_D) &= \int_{r_0}^{\infty} u_z^{\text{impact}}(\mathbf{r}_0) J_n(kr_0) \, dr_0 \\ &= \frac{4\pi R_D^2 D_C}{R_C^2 k^2} [J_2(kR_D) - k(R_D^2 - R_C^2)J_1(kR_D)]/2R_D \end{aligned} \quad (4)$$

Naturally, $u_z^{\text{surf}}(\mathbf{r},t=0) = u_z^{\text{impact}}(\mathbf{r})$. The bottom row of Figure 1 plots excitation function $|kF(k,R_C,R_D)|$ for lipless and lipped cavities. Impact tsunami have many spectral holes. We will see shortly that, due to the nature of tsunami dispersion, maximum tsunami amplitude appears near to the wavenumber of the first peak, $k_{\text{max}}=2/(2.11R_C)$. Wavelengths at peak tsunami amplitude correspond closely with the diameter of the impact cavity. Peak amplitude tsunami travel at group velocity

$$u(k_{\text{max}},h) = c(k_{\text{max}}) \left(\frac{1}{2} + k_{\text{max}} h / \sinh(2k_{\text{max}} h) \right), \quad (5a)$$

arrive at time $t_{\text{max}} = r/u(k_{\text{max}},h)$, and have frequency

$$\omega_{\text{max}} = [gk_{\text{max}} \tanh(k_{\text{max}} h)]^{1/2} \quad (5b)$$

Tsunami disperse normally with longer waves traveling faster than shorter waves. For $h=4$ km, (5a) and (5b) predict group velocities of 413, 238, and 159 km/h and periods of 123, 81, and 57 s for wavelengths of 20, 10 and 5 km.

In the far field (3) becomes

$$u_z^{\text{surf}}(\mathbf{r},t) = \int_0^{\infty} \sqrt{\frac{k}{2\pi^3 r}} dk F(k,R_C,R_D) \cos(kr - \omega(k)t - \pi/4) \quad (6)$$

The $1/\sqrt{r}$ term tracks tsunami amplitude loss due to geometrical spreading on a flat earth. Unless cavity outer radius $R_D \gg h$ (i.e. long-waves), frequency dispersion causes tsunami to decay much faster than $1/\sqrt{r}$. Dispersion “pulls apart” the initial tsunami pulse and further attenuates the waves. In fact, if R_D is smaller than or comparable to h , the combined effect of geometrical spreading and frequency dispersion cuts tsunami amplitudes nearly as $1/r$.

Tsunami Energy.

Tsunami (2) or (3) has total energy

$$E_T = (1/2) \rho_w g \int_r \mathbf{dr} [u_z^{\text{surf}}(\mathbf{r},t)]^2$$

$$E_T = (1/2) \rho_w g (D_C R_D)^2 [1 - R_D^2/R_C^2 + R_D^4/3R_C^4] \quad (7)$$

If $R_D=R_C$ (all water ejected), (7) is

$$E_T = (1/6) \rho_w g (D_C R_C)^2 \quad (8)$$

and if $R_D=\sqrt{2}R_C$ (all water deposited into lip), (7) is

$$E_T = (1/3) \rho_w g (D_C R_C)^2 \quad (9)$$

exactly twice as large as (8). Water deposited on the cavity lip adds as much energy to the tsunami as the cavity itself. The additional energy however, being composed of waves shorter in length than the cavity diameter, travels slowly and does not increase peak tsunami amplitude.

By necessity, some fraction η , of the kinetic energy E_I of the impactor goes into making the tsunami

$$E_T = \eta E_I = (1/2) \rho_I (4/3) R_I^3 V_I^2 \quad (10)$$

The energy conversion fraction may be constant, or a function of the properties of the impactor or the impacted material. With (7) and (10), initial cavity depth D_C can be restated in terms of η , and the density, radius, and velocity of the impactor

$$D_c = 2V_I \left(\frac{R_I^3}{3} \frac{\rho_I}{\rho_W} g R_D^2 [1 - R_D^2/R_C^2 + R_D^4/3R_C^4] \right)^{1/2} \quad (11)$$

Initial Cavities Shape Specifics.

From this point onward we specialize to initial transient cavities where all of the water has been deposited into the lip, ($R_D = \sqrt{2} R_C$) so there is no net water loss. In this case (11) becomes

$$D_c = (2 \frac{R_I^3 V_I^2}{g R_C^2})^{1/2} \quad (12)$$

Additionally, we envision a general relationship between cavity depth and radius as

$$D_c = q R_C \quad (13)$$

Here, q and α may vary with the properties of the impactor or impacted material. Placing (13) into (12) and solving for the diameter of the cavity ($d_c = 2R_c$) reveals

$$d_c = 2R_I \left(2\epsilon \frac{V_I^{2\delta}}{g R_I} \frac{\rho_I^{1/3}}{\rho_W} \frac{\rho_W^{1/3-\delta}}{\rho_I} \frac{1}{q R_I^{\alpha-1}} \right)^{2\delta} \quad (14)$$

where $\epsilon = 1/2(1 + \alpha)$. The well-known scaling rule for crater diameter of *Schmidt* and *Holsapple* (1982) constrains (14)

$$d_c^{S-H} = 2R_I \frac{1}{3.22} \frac{V_I^{2\beta}}{g R_I} \frac{\rho_I^{1/3}}{\rho_T} \frac{C_T}{1.24} \quad (15)$$

Parameters β and C_T depend on target properties. Equations (14) and (15) reconcile if the Schmidt-Holsapple parameter has a physical connection to the aspect ratio of the crater (i.e. $\alpha = 1/(2\beta) - 1$ in (13)) and if the impact energy conversion factor holds rather constant at $1/(2 \times 3.22) \sim 15\%$ for our lipped cavities. Laboratory impact experiments in water constrain $\beta = 0.22$, $\alpha = 1.27$ and $C_T = 1.88$. (For fixed q , materials with smaller β produce deeper transient cavities for a given diameter.) Equating the braced terms in (14) and (15) gives $q = 0.10, 0.083$ and 0.054 for impactors of density 3 gm/cm^3 and radii of 50, 100 and 500 m, respectively. With q and $\alpha = 1/(2\beta) - 1$, (13) associates a cavity depth with a Schmidt-Holsapple crater diameter (see Table 1).

The ratio of cavity diameter to cavity depth found by this approach (see Figure 2) slowly varies from

R_I (m)	diameter d_c	depth D_c	d_c/D_c	E_T GTon
25	1967	785	2.51	0.00145
50	3378	1291	2.62	0.0116
100	5800	2126	2.73	0.0929
125	6903	2497	2.76	0.117
150	7958	2847	2.80	0.313
200	9960	3502	2.84	0.743
250	11853	4113	2.88	1.45
300	13665	4690	2.91	2.51
400	17103	5769	2.96	5.94
500	20354	6774	3.00	11.6

Table 1. Cavity diameter and depth in meters as found from (13) and (14,15) versus impactor radius. Here $V_I = 20 \text{ km/s}$ and $\rho_I = 3 \text{ gm/cm}^3$. E_T is tsunami energy in Gigatons of TNT. Impactor energy is $E_T/0.155$

2.5:1 to 3:1 with impactor radii spanning 25 to 500 m. *Crawford* and *Mader* (1998), running Sandia's CTH shock physics code, obtained the same tendency for deeper and narrower cavities to be dug by smaller impactors. Figure 3 pictures cavity at $T = 25\text{s}$ from an impact of a 250 m radius asteroid ($V_I = 20 \text{ km/s}$, $\rho_I = 3.32 \text{ gm/cm}^3$) as computed by *Crawford* and *Mader* (1998). Overlaid is our idealized parabolic cavity (2) with a depth and diameter (4182 m, 12261 m) determined by equations (13) and (14,15) under the same impactor conditions. Apart from details of the lip, the cavities have remarkably similar character. This agreement suggests to us that the cavity shape idealization and the energy arguments above have solid footing.

To cap this section, consider a simplification common in the literature (cf. *Melosh* 1989) -- that of fixing the diameter to depth ratio of transient cavities. For a constant ratio of 3:1, $q = 2/3$, $\alpha = 1$, and cavity depth (12) reduces to

$$D_c = d_c/3 = Q R_I^{3/4}; \quad Q = (8 \frac{V_I^2}{9} \frac{\rho_I}{\rho_W} g)^{1/4} \quad (16)$$

Impact Tsunami Propagation.

Figures 4 and 5 plot cross-sections of expanding rings of tsunami waves induced by the impact of a 200 m diameter asteroid ($\rho = 3 \text{ g/cm}^3$) at 20 km/s as computed by equations (3) and (13-15). Note the strong effects of frequency dispersion in pulling apart the initial impact cavity and the correspondence of peak tsunami amplitude with waves of length equal to the cavity diameter. Waves longer than the cavity diameter arrive before the peak; shorter waves arrive after.

Figure 6 pictures the time history of the tsunami in Figure 5 at 10 to 600 km distance from the impact. Time reads from the left to right in minutes. The red arrows indicate the arrival time $[t_{\max} = r/u(k_{\max}, h)]$ of waves of length $2.11R_c$. The agreement of t_{\max} with the actual arrival time of the maximum height waves again confirms that the wavelength associated with peak tsunami height equals the initial cavity diameter. Note the strong dispersion and “scalping” due to the spectral holes in the impact cavity. The scallops arrive subsequent to the maximum peak so they play no role in tsunami hazard as defined below.

Maximum tsunami height.

Our reference to tsunami hazard concerns u_z^{\max} , the maximum tsunami height. Primarily, maximum tsunami height computed from (3) and (13-15) depends upon impactor radius R_1 and distance r . By assembling many dozen measurements of u_z^{\max} from plots like Figure 6, we find that $u_z^{\max}(r, R_1)$ can be approximated as

$$u_z^{\max}(r, R_1) = D_c \frac{1}{1+r/R_c} e^{1/2 + (\chi_1 - 1/2) e^{-\chi_2 R_c / h}} \quad (17)$$

Parameters $\chi_1 = 1.075$ and $\chi_2 = 0.035$ fall from least square fitting of the measurements (dots in Figure 6). Approximation (17) was motivated by the facts that $u_z^{\max}(r, R_1) \approx D_c$ as $r \rightarrow 0$; $u_z^{\max}(r, R_1) \approx (1/r)^{1/2}$ if $R_c \gg h$ (see equation (6)); and $u_z^{\max}(r, R_1) \approx (1/r)^{\chi_1}$ if $R_c \ll h$. Figure 7 graphs raw tsunami attenuation (17). The curves trace maximum tsunami height versus distance for asteroid radii between 1 and 500 meters and ocean depths of 1, 3 and 6 km. There is little dependence of attenuation on ocean depth for impactors smaller than about 200 m radius.

We intend to use (17) in place of full tsunami theory to calculate tsunami hazard. To the extent that the assumptions supporting the underlying theory (equations 1c, 2, 13-15) are sound, so too is the approximation. Certain special circumstances however, need to be aired. For instance, what should be done if the cavity depth exceeds the depth of the ocean at the impact site? According to Table 1 and (17), an asteroid of 100 m radius impacting a shallow sea of even 1 m depth induces a tsunami of 2126 m height. Is this reasonable? We think not. Most likely, an initial impact tsunami can not be higher than the ocean depth, regardless of

cavity depth. Accordingly, we restrict (17) with a leading amplitude factor being the lesser of ocean depth or calculated cavity depth

$$u_z^{\max}(r, R_1) = \min(D_c, h) \frac{1}{1+r/R_c} e^{1/2 + (\chi_1 - 1/2) e^{-\chi_2 R_c / h}} \quad (18)$$

Table 1 indicates that only impactors greater than 250 meters radius for cavities that “bottom out” in the mid-ocean, so mostly (17) and (18) offer no distinction. The limits in equation (18) activate largely for impacts on shallow continental shelves.

Shoaling Correction.

Equation (3) that led to (18) supposes oceans of constant depth. Toward shore, real oceans shallow and the waves carried on them amplify. Often, the processes of wave amplification are lumped and labeled “run-up”. Run-up has linear and non-linear elements. First order ray theory well-describes the linear elements -- refraction and shoaling. For parallel rays, the theory (Dingemans, 1997) gives

$$S_L(k_{\max}, h_s, h) = \frac{u(\omega_{\max}, h)}{u(\omega_{\max}, h_s)} e^{1/2} = \frac{u(k_{\max}, h)}{u(k(\omega_{\max}, h_s), h_s)} e^{1/2} \quad (19)$$

In our hazard calculations for u_z^{\max} , shoaling correction (19) multiplies the right hand side of (18). Shoaling amplification depends on the ratio of group velocity at the impact-site and the coast-site (ocean depth h and h_s , respectively) evaluated at the frequency associated with the peak tsunami height (5b). Note that only for long waves ($d_c \gg h$) does $u(k_{\max}, h) = (gh)^{1/2}$, $u(k_{\max}, h_s) = (gh_s)^{1/2}$, and (19) reduce to Green’s Law, $S_L = (h/h_s)^{1/4}$. Most impact tsunami do not classify as long waves.

Figure 8 plots (19) as a function of coast-site depth for typical initial cavity diameters of 2, 5, 10, 15 and 20 km (see Table 1), and ocean impact depths of 1, 3 and 6 km. The linear run-up factor S_L , falls between 2 and 5 over a wide range of conditions. Of course, equation (19) depends on linear theory, so it can not take the wave all the way to shore where h_s vanishes. We carry tsunami only to depth $h_s = u_z^{\text{crit}}$, which is several, to several tens of meters (see Section 3 below).

Equations (18) and (19) comprise linear amplitude theory for tsunami rays propagating out from the impact like spokes on a wheel. Topographic bending of the rays as they propagate from source to shore makes actual amplitudes locally larger or smaller. When viewed regionally however, refraction effects average out. Only a finite amount of wave energy exists to disperse, so concentrating it at one site, by necessity, robs it from another. Non-linear aspects of run-up, the actual breaking of the wave and disposition in water shallower than u_z^{crit} are highly dependent upon local topography and wave history. Because of this, we ignore non-linear shoaling amplifications entirely.

3 TSUNAMI HAZARD THEORY

Probabilistic tsunami hazard calculations parallel those that have been developed in seismic hazard analysis [e.g. Ward, 1996]. Hazard analysis keys on u_z^{crit} , a specified tsunami amplitude for which the probability of exceedence is desired. u_z^{crit} might be 2 m, for regions with low risk tolerance (e.g. shallow coastal flats) or maybe 10 m, for regions with a high risk tolerance. Inserting distance $r=|\mathbf{r}_s-\mathbf{r}_0|$ between coastline and impact sites \mathbf{r}_s and \mathbf{r}_0 , into (18) times (19), and setting the left side equal to u_z^{crit} will return a minimum, or critical cavity depth D_c such that the maximum tsunami height meets or exceeds u_z^{crit} . Call this $D_c^{\text{crit}}(r, u_z^{\text{crit}})$ or $R_1^{\text{crit}}(r, u_z^{\text{crit}})$ because we can relate cavity diameter to impactor radius from (13-15). Any impact at distance r with impactor radius greater than or equal to $R_1^{\text{crit}}(r, u_z^{\text{crit}})$ will exceed the hazard threshold of u_z^{crit} .

Let $n(R_1)$ be the annual rate of impacts of bodies of radius between R_1 and R_1+dR_1 per square meter of ocean. Because we presume to know the annual rate of falls of all sizes, the annual rate of falls that exceed our threshold is

$$N(\mathbf{r}_s, \mathbf{r}_0, u_z^{\text{crit}}) = \int_{R_1^{\text{crit}}(r, u_z^{\text{crit}})} n(R_1) dR_1 \quad (20)$$

$N^{-1}(\mathbf{r}_s, \mathbf{r}_0, u_z^{\text{crit}})$ gives the mean recurrence interval of exceedence at coast-site \mathbf{r}_s for the square meter of ocean at \mathbf{r}_0 . To get the total rate, integrate (20)

$$N(\mathbf{r}_s, u_z^{\text{crit}}) = \int_{\mathbf{r}_0(\mathbf{r}_s)} dA(\mathbf{r}_0) N(\mathbf{r}_s, \mathbf{r}_0, u_z^{\text{crit}}) \quad (21)$$

The domain of integration covers all ocean points $\mathbf{r}_0(\mathbf{r}_s)$ that are intervisible and unobstructed from \mathbf{r}_s . The double integration (20), (21) might be made more efficient by reversing the order

$$N(\mathbf{r}_s, u_z^{\text{crit}}) = \int_0 n(R_1) dR_1 \int_{\mathbf{r}_0(\mathbf{r}_s)} dA(\mathbf{r}_0) H(\mathbf{r}_s, \mathbf{r}_0, u_z^{\text{crit}}, R_1) \quad (22)$$

The “hit” function $H(\mathbf{r}_s, \mathbf{r}_0, u_z^{\text{crit}}, R_1)$ equals 1 if an impactor of radius R_1 falling at $\mathbf{r}_0(\mathbf{r}_s)$ generates a tsunami greater than u_z^{crit} at \mathbf{r}_s . It equals 0 otherwise. Either way, in time interval T , the Poissonian probability of one or more impact tsunami arriving at \mathbf{r}_s that exceed u_z^{crit} in amplitude is

$$P(\mathbf{r}_s, T, u_z^{\text{crit}}) = 1 - e^{-N(\mathbf{r}_s, u_z^{\text{crit}})T} \quad (23)$$

Probability (23) is site-specific, because rate (21) or (22) is. We aspire to map $P(\mathbf{r}_s, T, u_z^{\text{crit}})$ along the coastlines of the world.

Inclusion of Uncertainty.

The full worth of a probabilistic approach to hazard derives from its ability to incorporate uncertainty in both the asteroid sources and in the tsunami attenuation/propagation model. That is, probabilistic hazard can account for the distribution of λ , V_1 and V_1 for impact bodies of given R_1 , and for uncertainty in run-up factor (19). Let random variable $U_z^{\text{max}}(r, R_1)$ be the actual tsunami height at distance r from an impactor of radius R_1 . $U_z^{\text{max}}(r, R_1)$, of course, might differ significantly from its expected value $u_z^{\text{max}}(r, R_1)$. Computing probability $P[U_z^{\text{max}}(r, R_1) > u_z^{\text{crit}}]$ allows consideration to be made for “rogue” impactors and bathymetric conditions, that by chance, produce tsunamis larger or smaller than u_z^{crit} at distance r than would be estimated by the mean values of λ , V_1 and V_1 and factor (19).

Suppose that $P[U_z^{\text{max}}(r, R_1)]$ follows a Weibull distribution

$$P[U_z^{\text{max}}(r, R_1) = u] = \lambda[\lambda u]^{1/\nu-1} e^{-[\lambda u]^{1/\nu}} \quad (24)$$

where

$$\lambda = \frac{(1 + \nu)}{u_z^{\max}(r, R_I)}$$

and Γ is the gamma function (see Figure 9, top). The expected tsunami height $u_z^{\max}(r, R_I)$

$$E[U_z^{\max}(r, R_I)] = \int_0^{\infty} [\lambda u]^{1/\nu} e^{-[\lambda u]^{1/\nu}} du = u_z^{\max}(r, R_I)$$

equals (18) times (19). The standard deviation in height that includes variations both due to impactor parameters R_I and run-up R is

$$\begin{aligned} SD[U_z^{\max}(r, R_I)] &= \sigma u_z^{\max}(r, R_I) = \sqrt{\sigma_I^2 + \sigma_R^2} u_z^{\max}(r, R_I) \\ &= \frac{\sqrt{(1 + 2\nu) - \nu^2(1 + \nu)}}{(1 + \nu)} u_z^{\max}(r, R_I) \end{aligned} \quad (25)$$

Generally σ_I , and rate (20) becomes

$$N(\mathbf{r}_s, \mathbf{r}_0, u_z^{\text{crit}}) = \int_0^{\infty} P[U_z^{\max}(r, R_I) > u_z^{\text{crit}}] n(R_I) dR_I \quad (26)$$

with

$$P[U_z^{\max}(r, R_I) > u_z^{\text{crit}}] = e^{-[\lambda u_z^{\text{crit}}]^{1/\nu}}$$

Naturally if $u_z^{\max}(r, R_I) \gg u_z^{\text{crit}}$ or $u_z^{\max}(r, R_I) \ll u_z^{\text{crit}}$ then $P[U_z^{\max}(r, R_I) > u_z^{\text{crit}}] \rightarrow 1$ or 0 respectively. Note that the lower limit of integration in (26) equals zero not $R_I^{\text{crit}}(r, u_z^{\text{crit}})$. Because of uncertainty, smaller impactors may account for a larger proportion of hazard than might be expected. [In practice, the destructive effects of atmospheric entry impose an effective lower limit on impactor size. See “rate loss” discussion below.] In any case, if the uncertainty σ_I goes to zero, then $e^{-[\lambda u_z^{\text{crit}}]^{1/\nu}}$ in (26) collapses to a Heaviside step function centered at u_z^{crit} and the equation reverts to (20).

Variability in maximum tsunami height resulting from refraction and non-linear run-up can be quite large. We guess that the standard deviation σ_R of maximum tsunami height due to variations in refraction and non-linear run-up reach 100% of the mean wave height,

$$\sigma_R = 1.0 u_z^{\max} \quad (27)$$

4 ASTEROID IMPACT STATISTICS

Rate Density.

For cumulative impact rate density as a function of impactor radius, we consider a power law

$$n_{>}(R_I) = a R_I^{-b} \quad (28)$$

The differential rate density needed in (25) is

$$n(R_I) = ab R_I^{-b-1} \quad (29)$$

Constants a and b in (28) and (29) pertain to the size of impactors of interest, namely $30 < R_I < 500$ m. The flux distribution of bolides of this size is poorly constrained; however, reasonable information exists at either end of the range. At the small end, *Nemtchinov et al.* (1997) report that geostationary satellites observed globally, over a 22 month span, approximately 25 exploding meteors per year in the energy range from 0.25 to 4 kt TNT ($0.75 \text{ m} < R_I < 1.19 \text{ m}$, assuming $V_I = 20 \text{ km/s}$ and $\rho_I = 3 \text{ gm/cm}^3$). At the large end, *Shoemaker et al.* (1990) and *Toon et al.* (1994) estimate that “on average”, a 1 km [diameter] or larger object strikes the Earth once per 100,000 or 300,000 years respectively.

In absence of a firmer constraint, we select constants a and b such that (28) runs through the *Nemtchinov et al.* (1997) numbers at small impactor radius and *Shoemaker et al.*'s (1990) rate at large radius, i.e.

$$a = 3.89 \times 10^{-14} \text{ m}^{1/3}/\text{y}; \quad b = 7/3$$

Figure 10 shows that this selection generates one Earth-striking impactor $R_I > 500$ m in 100,000 years, one $R_I > 50$ m in 464 years, one $R_I > 5$ m in 2.2 years, and twenty $R_I > 1$ m annually. Obviously, bolide flux is a weak link in hazard assessment. In the next decade, searches such as Spacewatch, NEAT and LINEAR hold high hope for refining the small asteroid census.

In Section 5 we calculate 1000 year Poissonian probabilities of experiencing impact tsunami of heights $u_z^{\text{crit}} = 2$ to 50 m. To put these numbers in perspective, first consider the likelihood of being “hit on the head” (i.e. being inside of new impact cavities of the same depths as the proposed u_z^{crit}). In this case, the integral involving the hit function in (22) reduces to the area of the cavity

$$N(\mathbf{r}_s, u_z^{\text{crit}}) = (\pi/4) \int_{R_I^{\text{crit}}(u_z^{\text{crit}})} d_c^2(R_I) n(R_I) dR_I$$

and lower limit returns to $R_I^{\text{crit}}(u_z^{\text{crit}})$ the smallest impactor capable of making a cavity of depth u_z^{crit} . To keep it simple let's use (16) with (29),

$$\begin{aligned} N(\mathbf{r}_s, u_z^{\text{crit}}) &= (21\pi a Q^2 / 4) \int_{R_I^{\text{crit}}(u_z^{\text{crit}})} \frac{dR_I}{R_I^{11/6}} \\ &= 63\pi a Q^2 / 10 [R_I^{\text{crit}}(u_z^{\text{crit}})]^{5/6} \quad (30) \\ &= 63\pi a Q^{28/9} / 10 (u_z^{\text{crit}})^{10/9} \end{aligned}$$

because $u_z^{\text{crit}} = D_c^{\text{crit}} = Q(R_I^{\text{crit}}(u_z^{\text{crit}}))^{3/4}$. If $\rho = 0.155$, $V_I = 20$ km/s, $\rho_I = 3$ gm/cm³, $\rho_w = 1$ gm/cm³, and $Q = 64.1$ m^{1/4}, 1000 year probabilities (23) of a direct hit are

$$\begin{aligned} P(1000 \text{ y, } 2 \text{ m}) &= 0.0149\% \\ P(1000 \text{ y, } 5 \text{ m}) &= 0.00538\% \\ P(1000 \text{ y, } 10 \text{ m}) &= 0.00249\% \\ P(1000 \text{ y, } 15 \text{ m}) &= 0.00159\% \quad (31) \\ P(1000 \text{ y, } 25 \text{ m}) &= 0.000900\% \\ P(1000 \text{ y, } 50 \text{ m}) &= 0.000417\% \end{aligned}$$

As we shall see, these probabilities are dwarfed by the probability of being overrun by a distantly generated tsunami of the same height.

Rate loss due to the atmosphere.

Rate densities (28) and (29) correspond to impactor flux at the top of the atmosphere. In transit to the Earth surface, smaller objects tend to fragment and disintegrate, so impactor flux at the top of the atmosphere does not equal the flux at sea level where tsunamis are born. We account for atmospheric losses by including a high pass filter function $F_{\text{atm}}(R_I)$ in all integrals over impactor radius

$$\begin{aligned} F_{\text{atm}}(R_I, R_I^{\text{burn}}, R_I^{\text{survive}}) &= 0; \quad R_I < R_I^{\text{burn}} \quad (32) \\ &= .5[1 - \cos(\pi \frac{R_I - R_I^{\text{burn}}}{R_I^{\text{survive}} - R_I^{\text{burn}}})]; \quad R_I^{\text{burn}} < R_I < R_I^{\text{survive}} \\ &= 1; \quad R_I > R_I^{\text{survive}} \end{aligned}$$

Filter (32) presumes that all impactors of radius less than R_I^{burn} burn up in transit while all impactors of ra-

dius greater than R_I^{survive} pass unscathed. The flux of impactors of intermediate size cosine-taper from zero to one. *Toon et al. (1994)* note that stony asteroids smaller than ~65 m radius lose more than half their energy to airburst. $R=65$ m, then, is a suitable choice for the mid-point of the taper.

Uncertainties in Impactor Properties.

Impacting asteroids and comets occur with a range of densities, velocities and energy conversion efficiencies. Given probability density functions $P(\rho)$, $P(V_I)$, and $P(V_I)$ for these impactor properties, formulas (13) to (15) can find a probability distribution function for cavity depth $P(D_c)$. This in turn can be employed to estimate the uncertainty in maximum tsunami height due to variations in impactor properties.

Impactors come in several distinct populations: irons, stones, and comets. The most rigorous approach would account for the hazard of each of these populations individually, and assemble the total. In this paper however, we concentrate only on the dominant stony population. Figure 11 shows estimates of $P(\rho)$, $P(V_I)$, and $P(V_I)$ and the resulting cavity depth density $P(D_c)$. In this estimate, impactor density, velocity and energy conversion factors have a uniform probability of occurrence between $2 < \rho < 4$ gm/cm³, $0.10 < V_I < 0.20$ and $15 < V_I < 25$ km/s. Random and independently selected values from distributions $P(\rho)$, $P(V_I)$, and $P(V_I)$ produce the probability distribution of cavity depth $P(D_c)$ depicted as the jagged shape in the bottom panel. The red curve is a Gaussian distribution with mean D_c and standard deviation $0.11 D_c$. Equation (18) says that at distances large compared to the cavity depth $u_z^{\text{max}}(r, R_I) \approx D_c^2 / r$, so if D_c is a random Gaussian variable with standard deviation $0.11 D_c$, then $u_z^{\text{max}}(r, R_I)$ is approximately a random variable with standard deviation

$$\sigma = 0.22 u_z^{\text{max}} \quad (33)$$

σ quantifies the spread in maximum tsunami amplitude about the mean due to variations in impactor characteristics. Compared with the variations assigned to tsunami amplitude due to refraction and run-up (equation 27), σ is small. The combined effect of uncertainties (33) and (27) in exceedence rate (26), $\sigma = 1.02$ means that:

14% of all tsunamis actually beach at heights above

twice their mean size; and

40% of all tsunamis actually beach at heights below one-half their mean size (see Figure 9, bottom).

5 PROBABILISTIC HAZARD ASSESSMENT

Equations (13) to (15), (18) to (29), (32) and (33) present all of the ingredients to make a probabilistic assessment of impact tsunami hazard by integrating (26) and then (21). We evaluate hazard of two types: site-generic and site-specific. The first type selects ocean exposure and ocean depth-distance function $h(r)$, generic to all oceans. Site-specific hazard on the other hand, reads those conditions from maps.

Site-generic hazard.

Generic hazard imagines coastal sites exposed to $\theta_s = 90, 180, \text{ and } 360$ degrees of ocean with a depth-distance profile

$$h(r) = \max[u_z^{\text{crit}}, 200m(r/100km)] \quad r < 100km \quad (34)$$

$$h(r) = 200m + 4800m[1 - \exp(-r/250km)] \quad r > 100km$$

out to a maximum reach $r = r_{\text{max}}^{\text{reach}}$. An ocean depth profile fixes water depth at the impact site, a parameter appearing in shoaling correction (19). As discussed under the shoaling section, u_z^{crit} is the smallest depth permitted. Profile (34) has a shelf (<200m depth) out to 100 km distance, followed by a rapid descent to a uniform 5000 m deep (see Figure 12).

Table 2 lists the 1000-year Poissonian probability of one or more impact tsunami exceeding heights of 2 to 50 m at generic coast sites with 360, 180 and 90 degrees of exposure and $r_{\text{max}}^{\text{reach}}$ between 1,000 and 10,000 km. The top number in each row pair lists the probability without the reduction of impactor flux by the atmosphere. The bottom number accounts for these losses with filter (32) where $R_I^{\text{burn}} = 30$ m and $R_I^{\text{survive}} = 100$ m (see Figure 10). Without accounting for impactor flux loss through the atmosphere, a typical site with 180 degrees of exposure and a reach of 6,000 km, admits a 1-in-6 chance of one or more impact tsunami of 2 m height or greater in 1000 years. The likelihood drops to 1-in-23 for a 5 meter wave, and to 1-in-320 for a 25 meter wave. Including atmospheric flux losses, the same site can expect a 1-in-14 chance of

u_z^{crit}	$\theta_s = 360 \text{ degrees}$					
	1000	2000	4000	6000	8000	10000
2 m	12.01	18.30	26.76	32.60	36.88	40.06
	0.86	2.87	8.18	13.54	18.18	21.92
5	2.62	4.21	6.54	8.30	9.68	10.74
	0.64	1.72	3.85	5.61	7.02	8.12
10	0.81	1.34	2.14	2.75	3.23	3.61
	0.40	0.88	1.67	2.29	2.77	3.15
15	0.41	0.69	1.11	1.42	1.67	1.86
	0.27	0.54	0.96	1.28	1.53	1.72
25	0.17	0.30	0.48	0.61	0.71	0.78
	0.14	0.27	0.45	0.58	0.68	0.75
50	0.05	0.09	0.14	0.18	0.20	0.21
	0.05	0.09	0.14	0.17	0.20	0.21

u_z^{crit}	$\theta_s = 180 \text{ degrees}$					
	1000	2000	4000	6000	8000	10000
2 m	6.20	9.61	14.42	17.90	20.56	22.58
	0.43	1.45	4.18	7.01	9.55	11.64
5	1.32	2.13	3.33	4.24	4.96	5.53
	0.32	0.86	1.94	2.84	3.57	4.15
10	0.41	0.67	1.07	1.38	1.63	1.82
	0.20	0.44	0.84	1.15	1.40	1.59
15	0.21	0.34	0.55	0.71	0.84	0.94
	0.13	0.27	0.48	0.64	0.77	0.86
25	0.09	0.15	0.24	0.31	0.35	0.39
	0.07	0.13	0.22	0.29	0.34	0.38
50	0.03	0.05	0.07	0.09	0.10	0.11
	0.03	0.04	0.07	0.09	0.10	0.11

u_z^{crit}	$\theta_s = 90 \text{ degrees}$					
	1000	2000	4000	6000	8000	10000
2 m	3.15	4.93	7.49	9.39	10.87	12.01
	0.22	0.73	2.11	3.57	4.89	6.00
5	0.66	1.07	1.68	2.14	2.51	2.80
	0.16	0.43	0.98	1.43	1.80	2.10
10	0.20	0.34	0.54	0.69	0.82	0.91
	0.10	0.22	0.42	0.58	0.70	0.80
15	0.10	0.17	0.28	0.36	0.42	0.47
	0.07	0.14	0.24	0.32	0.38	0.43
25	0.04	0.07	0.12	0.15	0.18	0.20
	0.04	0.07	0.11	0.15	0.17	0.19
50	0.01	0.02	0.04	0.04	0.05	0.05
	0.01	0.02	0.03	0.04	0.05	0.05

Table 2. 1000 year Poissonian probability in percent, of one or more impact tsunami exceeding $u_z^{\text{crit}} = 2$ to 50 m hitting a generic coastal site with $\theta_s = 360$ degrees (top), 180 degrees (middle), or 90 degrees (bottom) of ocean exposure and reaches between $r_{\text{max}}^{\text{reach}} = 1,000$ and 10,000 km. The bottom number shows the probability after reduction of the impactor flux by the atmosphere. enduring a 2 meter wave or greater; 1-in-35 for a 5

meter wave, and 1-in-345 for a 25 meter wave. Atmospheric flux losses most strongly affect the likelihood of the smaller tsunami because these tend to be generated by smaller impactors. Naturally, larger or smaller exposure angles and reaches make for larger or smaller likelihood of exceeding any hazard threshold. Although the probabilities in Table 2 are not terribly high, they exceed the direct hit likelihood (31) by many hundred-fold. This testifies to the fact that tsunami carry impact energy to distances far beyond the initial cavity. When integrated over the Earth's coastlines, impact tsunami certainly entail a perceptible risk.

The total tsunami hazard listed in Table 2 distributes non-uniformly over impactor radius and impact distance. Figure 13 breaks down the total hazard (including atmospheric filtering) at a generic coast site versus impactor size. A break down reveals what size impactor is most responsible for the hazard at each tsunami size. The top panel shows the normalized exceedence rate density for thresholds of 2, 5, 10, 25 and 50 m. The peak contributor to tsunami greater than 5 meters, for example, are impactors of 110 m radius. Note how the peaks flatten and shift toward larger impactors as the threshold increases. The bottom panel graphs cumulative exceedence rate in percent for all impactors less than radius R. The dots mark the radius at which 90% of total exceedences derive from impactors of that size or less. For instance, 90% of all the tsunami greater than 10 m (25 m) amplitude striking the generic site come about from impacts of asteroids of 480 m (890 m) radius and less. The curves in Figure 13 indicate that impacts of bodies greater than 2 km diameter contribute little to our measure of hazard (1000 year interval, $u_z^{crit} < 50$ m).

Site-specific hazard.

The final step in this exercise evaluates impact tsunami hazard for actual sites by: a) running great circles radially outward over all azimuths from the site until striking land; b) reading ocean depth from 5x5 minute ETOPO bathymetry at each impact site so intervisible; and c) integrating (25) then (21). Figure 14 illustrates the concept for the six sites selected for analysis: San Francisco, New York, Tokyo, Hilo, Perth and Sydney. Ocean exposure varies considerably place to place. San Francisco faces 1.72×10^8 km² of potential impact area versus 0.64×10^8 km² for New York City. Hazard exceedence rates scale with exposure, but the relationship is not linear. Exposure to a distant square meter of ocean contributes less to hazard than does exposure to

u_z^{crit}	SFC	NYC	TOK	PRH	SYD	HLO
2 m	22.22	13.87	24.98	20.98	19.44	32.02
	12.01	5.58	11.65	8.90	8.84	15.34
5	5.47	3.19	6.15	5.07	4.68	8.25
	4.13	2.13	4.18	3.38	3.20	5.83
10	1.78	1.01	1.97	1.63	1.50	2.71
	1.54	0.83	1.60	1.32	1.23	2.27
15	0.90	0.51	0.99	0.82	0.75	1.38
	0.82	0.45	0.86	0.71	0.66	1.23
25	0.37	0.21	0.40	0.34	0.30	0.57
	0.35	0.20	0.37	0.31	0.28	0.54
50	0.10	0.06	0.11	0.09	0.08	0.16
	0.10	0.06	0.11	0.09	0.08	0.16

Table 3. 1000 year Poissonian probability in percent, of one or more impact tsunami exceeding $u_z^{crit} = 2$ to 50 m at six selected coastal sites: San Francisco California (SFC), New York City (NYC), Tokyo (TOK), Perth Australia (PRH), Sydney Australia (SYD) and Hilo Hawaii (HLO). The bottom number includes atmospheric flux losses. Compare these probabilities with the site-generic values in Table 2.

a close-in square meter because only large, hence rare, impactors generate a tsunami sizable enough to carry from the distant site. However, because the number of distant square meters exceeds the number of close-in square meters, the equation balances partly. Of the sites investigated, Hilo Hawaii has the largest hazard probability at 15.3% and 5.8% for one or more 2 and 5 meter waves respectively per 1000 year interval. New York City brings up the rear with 5.6% and 2.1%. These numbers include the effects of impactor flux losses by the atmosphere.

Region-specific hazard.

The site-specific probabilities in Table 3, generally are not independent in that a certain fraction of the exceedences at site pairs (San Francisco and Hilo, say) stem from the same impact. To determine region-specific hazard, let vector $\mathbf{C}=(\mathbf{c}_1, \mathbf{c}_2, \mathbf{c}_3, \dots, \mathbf{c}_n)$ contain n points \mathbf{c}_i that trace a specified stretch of coastline. The annual rate $N(\mathbf{C}, u_z^{crit})$ that impact tsunami with peak amplitude greater than or equal to u_z^{crit} strike *anywhere* on \mathbf{C} is

$$N(\mathbf{C}, u_z^{crit}) = \int_{\mathbf{r}_0} dA(\mathbf{r}_0) \int_{R_1^{crit}(\mathbf{D}_{min}(\mathbf{r}_0, \mathbf{C}), u_z^{crit})} n(R_1) dR_1 \quad (35)$$

Here,

$$\mathbf{D}_{min}(\mathbf{r}_0, \mathbf{C}) = \min[|\mathbf{c}_1 - \mathbf{r}_0|, |\mathbf{c}_2 - \mathbf{r}_0|, |\mathbf{c}_3 - \mathbf{r}_0|, \dots, |\mathbf{c}_n - \mathbf{r}_0|]$$

(36)

gives the closest distance from the impact site \mathbf{r}_0 to any intervisible and unobstructed coastal point. The domain of integration covers all ocean locations from where at least one of the \mathbf{c}_i can be seen. If \mathbf{r}_s is an element of \mathbf{C} , then rate (35) for the whole coastline must be greater than or equal to rate (21) for \mathbf{r}_s alone because $R_1^{\text{crit}}(D_{\min}(\mathbf{r}_0, \mathbf{C}), u_z^{\text{crit}}) \geq R_1^{\text{crit}}(r, u_z^{\text{crit}})$ for any \mathbf{r}_0 by virtue of the fact that $D_{\min}(\mathbf{r}_0, \mathbf{C}) \leq r = |\mathbf{r}_s - \mathbf{r}_0|$. On the other hand, (35) is less than the rate obtained simply by integrating (21) over all points \mathbf{C} because (35) does not “double count” single tsunami waves that top u_z^{crit} at more than one location along the coast.

6 COMPARISONS AND CAVEATS.

Comparisons.

Bearing in mind that impact tsunami may be the most likely asteroid hazard in human and economic terms, the literature reflects surprisingly little consensus about them. Consider two recent generation/propagation models for impact tsunami: *Hills et al.* (1994), and *Crawford and Mader* (1998). *Hills et al.* (1994) base their analysis upon empirical relations (*Glasstone and Dolan*, 1977) for the height of a deep water wave emanating from an underwater nuclear explosion of roughly 1 kt yield. By substituting the explosive yield of bombs in these relations with asteroid impact energy E_i , they calculate that asteroids 250 m in diameter impacting at 20 km/s ($E_i \sim 10^6$ kt) should produce deep water waves with 15 m amplitude at 1000 km distance. Proposing large tsunami runup factors of 10 to 25, they argue that relatively small asteroid impacts can wreak havoc to coastlines. Calculations by *Crawford and Mader* (1998) lead to very different conclusions. Their CTH shock physics code (for describing the hypervelocity impact) and ZUNI Navier-Stokes code (for modeling wave propagation) for the same 250 m diameter asteroid predict tsunami amplitudes less than 10 meters after only 60 km of travel, and imperceptible signals after 1000 km.

For comparison, our model offers (Formula 18, Table 1) a 7 m wave at 1000 km distance from the same 250 m diameter impactor. A 7 m tsunami is about half the size of *Hills et al.*, but much larger than *Crawford and Mader's*. Linearized runup theory (19), on the other hand, calls for smaller amplification than assumed by *Hills et al.*, so our waves arrive more modestly at shore. Being about 10 times less than *Hills et*

al. (1994) and perhaps 10 times greater than *Crawford and Mader* (1998), our predictions split the field.

Caveats.

Although we believe that the hazard assessments presented here improve current practice and break trail for future analyses, it is worthwhile to touch upon the major categories of uncertainty.

Cavity formation. As suggested by Figure 3, the parabolic form of transient impact cavities (2), and the energy based depth/diameter relations (13,14-15) tying impactor radius, velocity and density look to be sound. For any impactor, our cavity diameters reproduce exactly those from the well-founded Schmidt-Holsapple rule. Installation in (18) of the factor that limits initial tsunami height to the ocean depth is arbitrary, but it finds support in numerical simulations of impacts that bottom-out [*Crawford and Mader*, 1998]. Monster impacts that displace kilometers of oceanic crust are not handled here, but as Figure 12 shows, asteroids larger than 1000 m radius play little role in 1000 y hazard statistics for waves below 50 m. High pass tapering (32) probably covers adequately the effects of atmospheric ablation. Still, incorporation of energy losses for bodies smaller than one hundred meters could stand refinement, especially with respect to impactor composition -- iron and comet bolides survive ablation at smaller and larger radii than stones, respectively. Potential tsunami from powerful airbursts, such as the 1908 Tunguska explosion, are not considered.

Non-linear effects at early time. This paper employs classical, linear tsunami theory to compute exceedence probabilities. Linear theory assumes that wave amplitude is negligible compared to wavelength and ocean depth. Judging from Figures 4 and 7, these conditions look to be adequately satisfied excepting perhaps the first dozen seconds after impact. Figure 2 quotes initial cavity height-to-width ratios of about 1 to 3 – small, but maybe not negligible. Dave Crawford (*personal comm.* 1999) has suggested that, in the first moments of cavity evolution, the omission of certain non-linear terms in the equations of motion, stress-strain relation, or boundary conditions might explain why our tsunami height predictions are larger than those computed by *Crawford and Mader* (1998). We can not comment on the significance or relevance of non-linear effects in this application. Certainly a first step to address the issue calls for detailed ‘head-to-head’ comparisons of cavity evolution predicted from linear models (such as Figure 4) with various non-linear models under identical initial conditions. If by calculation and experiment,

a non-linear theory is found to better represent reality, then an updated tsunami attenuation law should replace (17) as the basis for the exceedence rate calculation (20).

Tsunami Propagation. Apart from the first moments after impact, uncertainties in propagating tsunami waveforms, given a cavity shape, certainly are small because the formative equations work for deep or shallow water, albeit of constant depth. Sophisticated propagation codes that evaluate tsunami refraction in variable depth oceans might be useful for site-specific hazard. Refraction however, being a zero sum game, is reasonably handled as we do as an additional uncertainty. Shoaling corrections are well-established, at least in the linear domain. The nonlinear components of runup in breaking waves and inundation of coastal planes (e.g. Hills *et al.*, 1994; Bretschneider and Wybro, 1977) however, comprise a gray area in hazard estimation that has yet to be illuminated widely.

Impactor statistics. This paper holds impactor density and velocity within about 25% of 3 gm/cm^3 and 20 km/s. The model's formalism well-incorporates these uncertainties. The effects of impactors drawn from distinct populations, say comets, have not yet been considered. Perhaps the weakest link in these hazard calculations is impactor flux. Although the $R_1^{-7/3}$ power law flux of stony asteroids reflects the best available information, the actual flux of Earth-crossing objects may differ by a factor of three. One could expect then, fluctuations of the same scale in the probabilities in Table 2 or Table 3. On the bright side, although impactor flux may be the largest uncertainty, it is one of the easiest features of the model to readjust as knowledge improves.

7 CONCLUSIONS

We investigate the generation, propagation, and probabilistic hazard of tsunami spawned by oceanic asteroid impacts. The process first links the depth and diameter of parabolic impact cavities to asteroid density, radius and impact velocity by means of elementary energy arguments and crater scaling rules. Linear tsunami theory monitors the evolution of initial parabolic impact cavities into sea surface waveforms at distant positions and times. The theory uses a uniform depth ocean, but otherwise holds for both long and short waves. After computing maximum wave amplitude at many distances for a variety of impactor sizes, we fit simplified attenuation relations that account both for geometrical spreading and frequency dispersion. Tsunami wavelengths that contribute to the peak am-

plitude coincide closely with the diameter of the transient impact cavity. For impactors smaller than a few hundred meters radius, cavity widths are less than or comparable to mid-ocean depths. As a consequence, dispersion increases the $1/\sqrt{r}$ long-wave decay rate to nearly $1/r$ for tsunami from these sources. In the final step, linear shoaling theory applied at the frequency associated with peak tsunami amplitude corrects for amplifications as the waves near land.

By coupling tsunami amplitude/distance information with the statistics of asteroid falls, the probabilistic hazard of impact tsunami are assessed in much the same way as probabilistic seismic hazard, by integrating contributions over all admissible impactor sizes and impact locations. Tsunami hazard, expressed as the Poissonian probability of being inundated by waves from 2 to 50 meter height in a 1000 year interval, is computed at both generic (generalized geography) and specific (real geography) sites. Importantly, hazards figured by this probabilistic approach can account for uncertainties in shoaling and impactor property variation, and can be broken down to assess the importance of impactor size distribution and impact location on total hazard.

A typical generic site with 180 degrees of ocean exposure and a reach of 6,000 km, admits a 1-in-14 chance of an impact tsunami of 2 meter height or greater in 1000 years. The likelihood drops to 1-in-35 for a 5 meter wave, and to 1-in-345 for a 25 meter wave. Calculated hazards for specific sites mimicked those for the generic sites. Hazard largely varies with the area of ocean exposed, although the relationship is not strictly linear. Of the sites investigated, Hilo Hawaii has the largest 1000-year hazard at 15.3 % and 5.8% for 2 and 5 meter waves respectively. Tokyo and New York have 1-in-24 and 1-in-47 chances of suffering an impact tsunami greater than 5 m in the next millennium. The lion's share of the hazard derives from impactors of moderate size. For example, 90% of all of the tsunami greater than 10 m amplitude striking the generic site come about from asteroids of 480 m radius and less. For our measure of hazard (1000 year interval, $u_z^{\text{crit}} < 50 \text{ m}$), impacts of bodies greater than 3 km diameter are of no concern.

Investigations of this style that merge proper tsunami theory with rigorous probabilistic hazard analysis advance considerably the science of impact tsunami forecasting and we envision continued refinement of this approach.

Acknowledgments: We thank Dave Crawford and Alan Hildebrand for their reviews. This work was partially supported by Southern California Earthquake Center Award 662703, NSF Contract EAR-9804970 (SNW) and by NASA's Planetary Geology and Geophysics Program (EA). Contribution 410? of the Institute of Tectonics, University of California, Santa Cruz CA, 95064. ward@uplift.ucsc.edu; asphaug@cosmic.ucsc.edu

REFERENCES.

- Alvarez, L.W., W. Alvarez, F. Asaro and H.V. Michel 1980. Extra-terrestrial cause for the Cretaceous-Tertiary extinction. *Science* **208**: 1095-1108.
- Ben-Menahem, A. and S.J. Singh 1981. *Seismic Waves and Sources*, Springer-Verlag, New York.
- Bretschneider, C.L. and P.G. Wybro 1977. Tsunami inundation prediction. In *Proc. Fifteenth Coastal Engr. Conf.*, ed. C.L. Bretschneider (NY: Am. Soc. Civ. Engr.), vol. 1, 1006-1024.
- Crawford, D.A. and C. Mader 1998. Modeling asteroid impact and tsunami. *Science of Tsunami Hazards* **16**, 21-30.
- Dingemans, M. W., 1997. *Water wave propagation over uneven bottoms, Part-1 linear wave propagation.*, World Scientific, Singapore.
- Gault, D.E. and C.P. Sonnett 1982. Laboratory simulation of pelegic asteroid impact. In *Geological Implications of Impacts of Large Asteroids and Comets on the Earth*, eds. L.T. Silver and P.H. Schultz, GSA Special Paper 190 (Boulder: GSA), pp. 69-72.
- Gersonde, R., Kyte, F.T., Bleil, U., Diekmann, B., Flores, J.A., Gohl, K., Grahl, G., Hagen, R., Kuhn, G., Sierro, F.J., Völker, D., Abelmann, A., and Bostwick, J.A. 1997. Geological record and reconstruction of the late Pliocene impact of the Eltanin asteroid in the Southern Ocean. *Nature* **390**, 357-363.
- Glasstone, S. and P.J. Dolan 1977. *The Effects of Nuclear Weapons*, 3rd ed. (Washington: US Govt. Printing Office)
- Hills, J.G., I.V. Nemtchinov, S.P. Popov and A.V. Terev 1994. Tsunami generated by small asteroid impacts. In *Hazards due to Comets and Asteroids*, ed. T. Gehrels (Univ. Arizona Press, Tucson), 779-790.
- Melosh, H.J. 1989. *Impact Cratering: A Geologic Process* (Oxford University Press)
- Nemtchinov, I.V., T.V. Loseva and A.V. Terev 1996. Impacts into oceans and seas. *Earth, Moon and Planets* **72**, 405-418.
- Nemtchinov, I.V., V.V. Svetsov, I.B. Kosarev, A.P. Golub, O.P. Popova, V.V. Shuvalov, R.E. Spalding, C. Jacobs and E. Tagliaferri 1997. Assessment of kinetic energy of meteoroids detected by satellite-based light sensors. *Icarus* **130**, 259-274.
- Roddy, D.J., S.H. Shuster, M. Rosenblatt, L.B. Grant, P.J. Hassig and K.N. Kreyenhagen 1987. Computer simulations of large asteroid impacts into oceanic and continental sites. *Int. J. Impact Eng.* **5**, 123-135.
- Schmidt, R.M. and K.A. Holsapple 1982. Estimates of crater size for large-body impacts: Gravitational scaling results. GSA Special Paper 190 (Boulder: GSA), 93-101.
- Smit, J. *et al.* 1996, in *The Cretaceous-Tertiary Event and Other Catastrophes in Earth History* (eds. Ryder, G., Fastovsky, D. and Gartner, S.), 151-182 (Geol. Soc. Am., Boulder)
- Shoemaker, E.M., R.F. Wolfe and C.S. Shoemaker 1990. Asteroid and comet flux in the neighborhood of Earth. In *Global Catastrophes in Earth History*, eds. V.L. Sharpton and P.D. Ward, GSA Special Paper 247 (Boulder: GSA), pp. 155-170.
- Toon, O.B., K. Zahnle, R.P. Turco and C. Covey 1994. Environmental perturbations caused by asteroid impacts. In *Hazards due to Comets and Asteroids*, ed. T. Gehrels (Univ. Arizona Press, Tucson), 791-826.
- Ward, S.N., 1994, A Multidisciplinary Approach to Seismic Hazard in Southern California, *Bull. Seism. Soc. Am.*, **84**, 1293-1309.

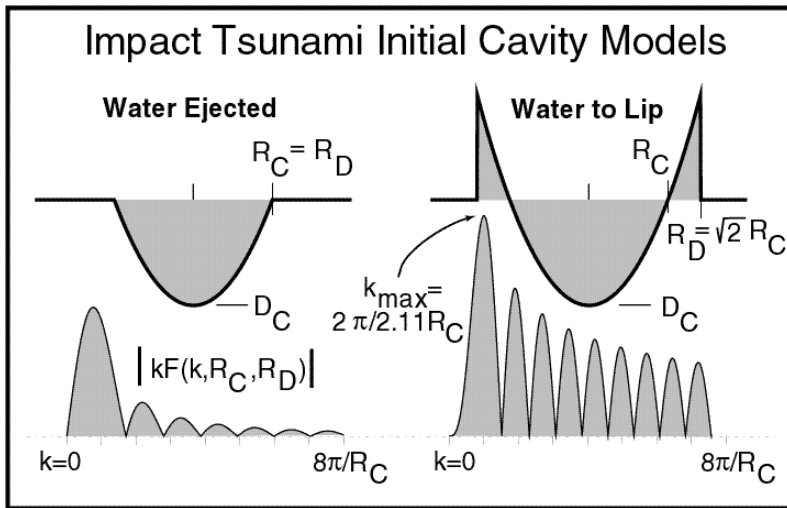


Figure 1. (Above) Cross section of impact cavities (2) without a lip and with a lip. (Below) wavenumber spectra of the cavities. The cavity with a lip has much stronger short wavelength components than does the cavity without a lip. The enhanced short wavelength spectra however, contributes nothing to maximum tsunami amplitude because that energy arrives subsequent to the tsunami peak.

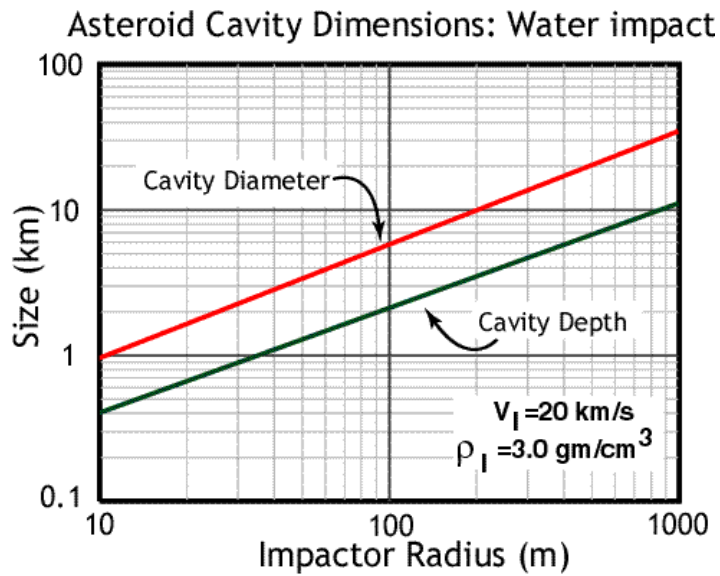


Figure 2. Plot of cavity diameter and depth versus impactor radius as computed from equations (13) and (14, 15).

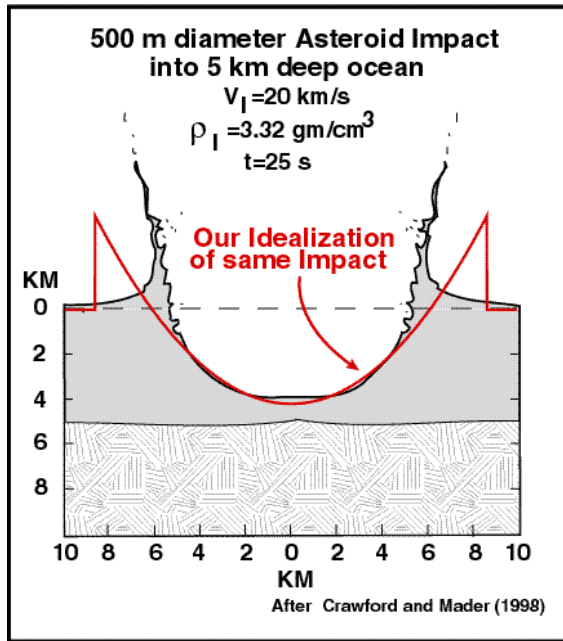


Figure 3. Comparison of Crawford and Mader's (1998) numerical simulation of a transient impact cavity and our parabolic shape idealization (2) with a depth and width derived from (13) and (14,15) using the same impactor parameters. Apart from the lip, the two cavities have similar character.

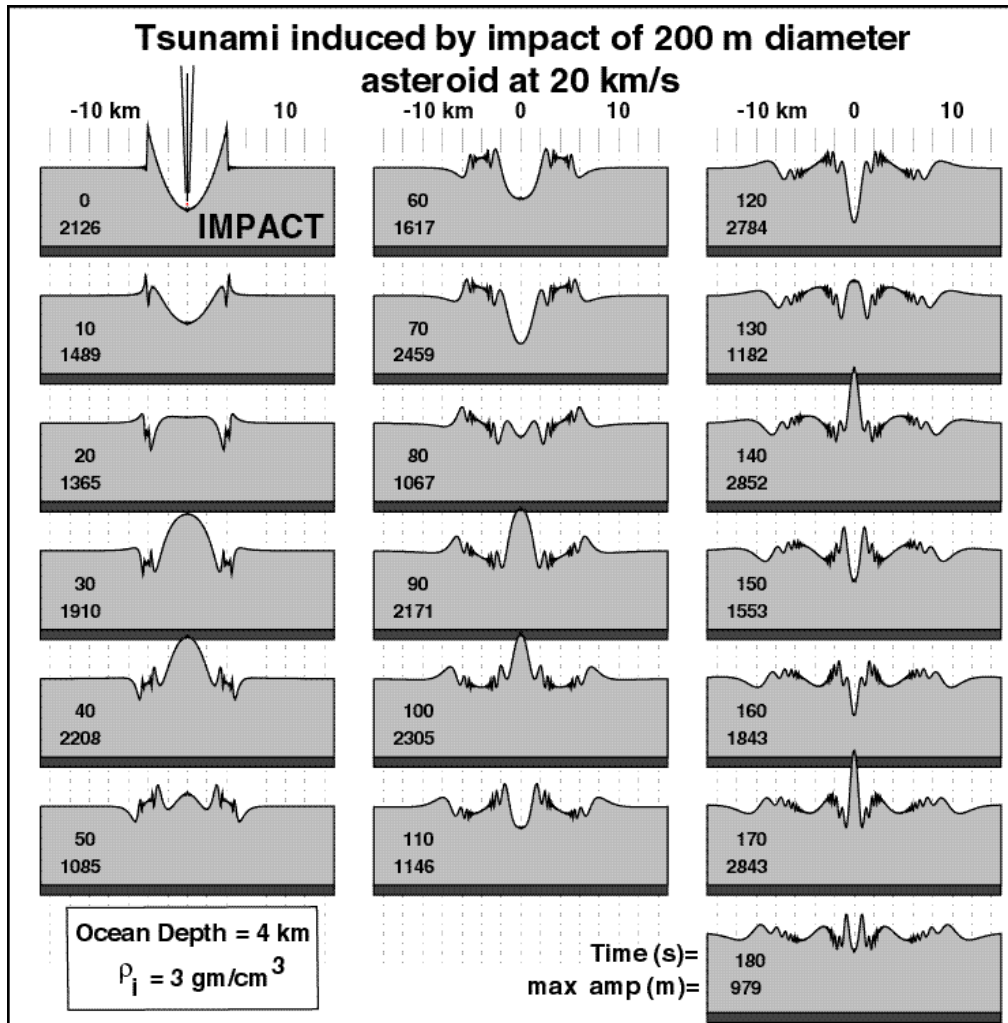


Figure 4. Tsunami induced by the impact of a 200 m diameter asteroid at 20 km/s as computed by equations (3) and (13-15). The waveforms (shown at 10 second intervals) trace the surface of the ocean over a 30 km cross section that cuts rings of tsunami waves expanding from the impact site at $x=0$. Maximum amplitude in meters is listed to the left.

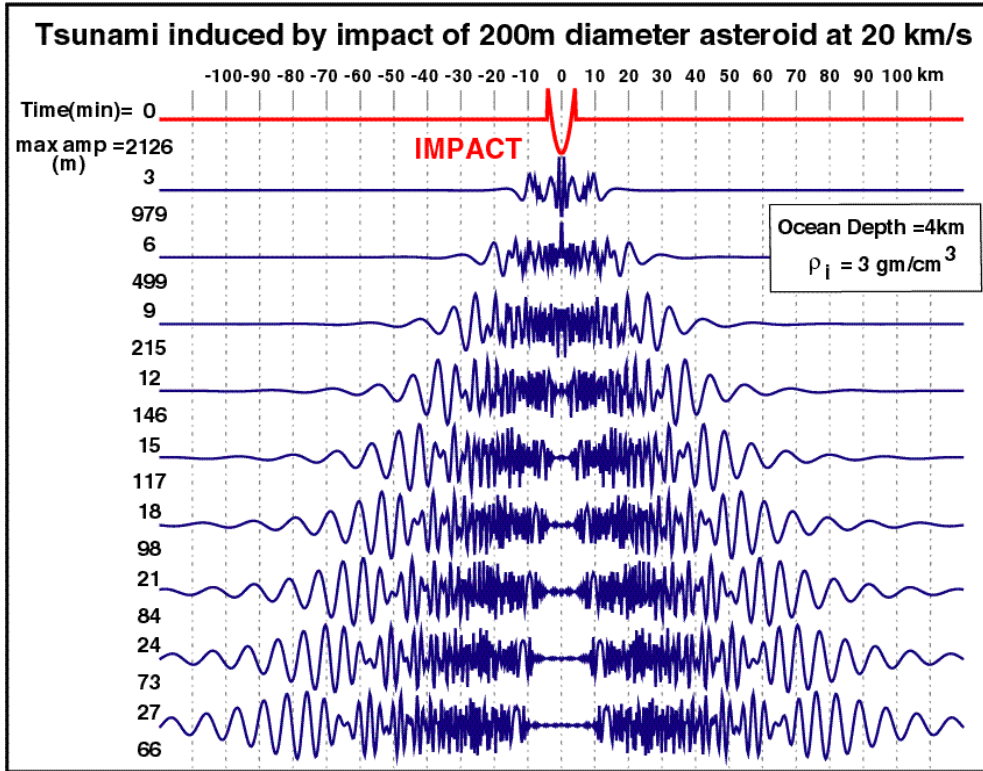


Figure 5. Tsunami induced by the impact of 200 m diameter asteroid at 20 km/s as computed by equations (3) and (13-15). The waveforms (shown at minute intervals) trace the surface of the ocean over 220 km cross section that cuts rings of tsunami waves expanding from the impact site at $x=0$. Maximum amplitude in meters is listed to the left. Peak tsunami amplitude located at the wavelength corresponding to the cavity diameter.

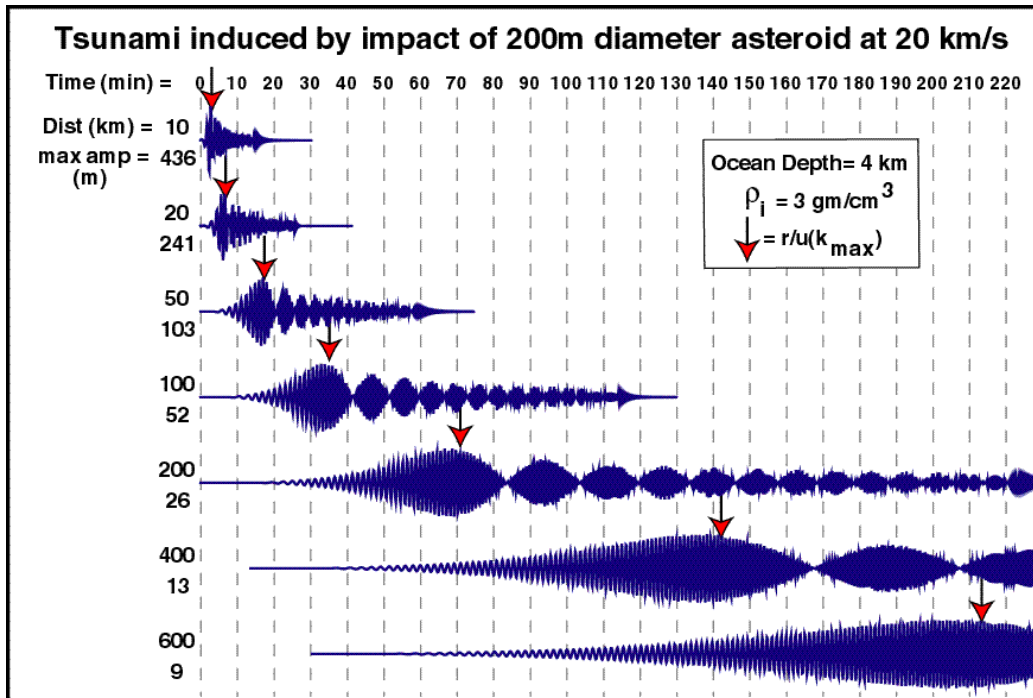


Figure 6. Tsunami induced by the impact of 200 m diameter asteroid at 20 km/s as computed by equations (3) and (13-15). Time varying waveforms are shown at fixed distances from 10 to 600 km from the impact. Time reads left to right from 0 to 220 minutes after impact. Maximum amplitude in meters is listed on the left. The red arrow marks the predicted arrival time $[t_{max} = r/u(k_{max})]$ of the maximum wave height. Maximum tsunami amplitude versus distance are shown in many plots like these are capsulized in Figure 7.

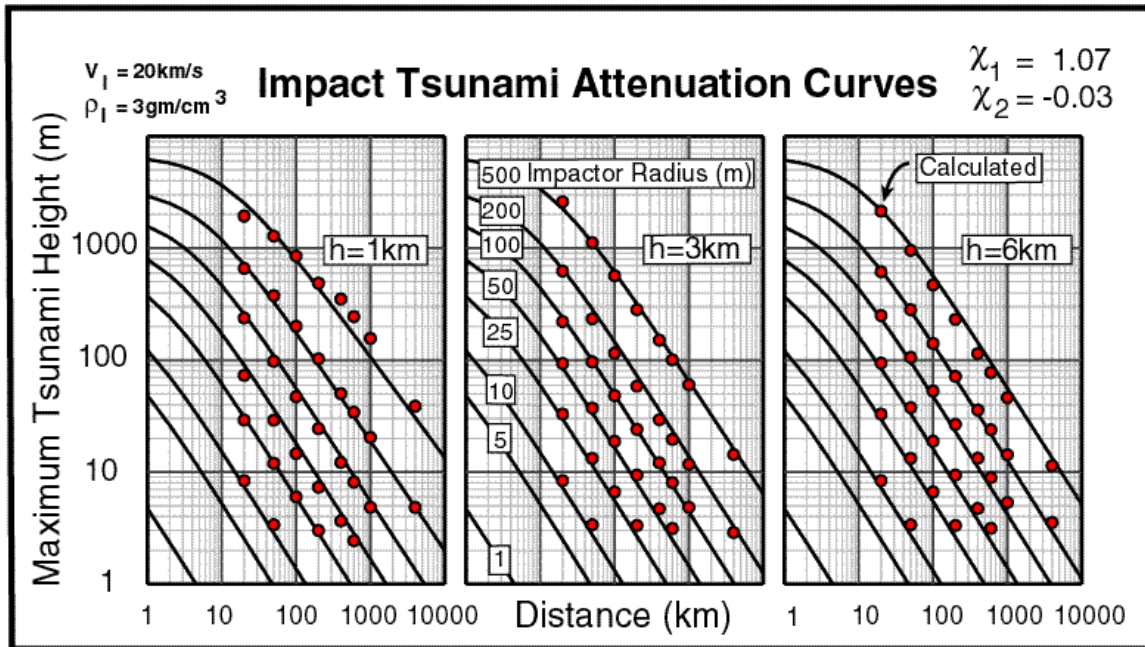


Figure 7. Raw tsunami attenuation curves from equation (17). The curves fit calculated maximum tsunami height (*dots*) versus distance for asteroid radii between 1 and 500 meters in oceans of 1, 3 and 6 km depth. Be aware that these curves do not apply for cases where cavity depth exceeds the ocean depth, nor do they contain corrections for impactor energy losses in the atmosphere or shoaling.

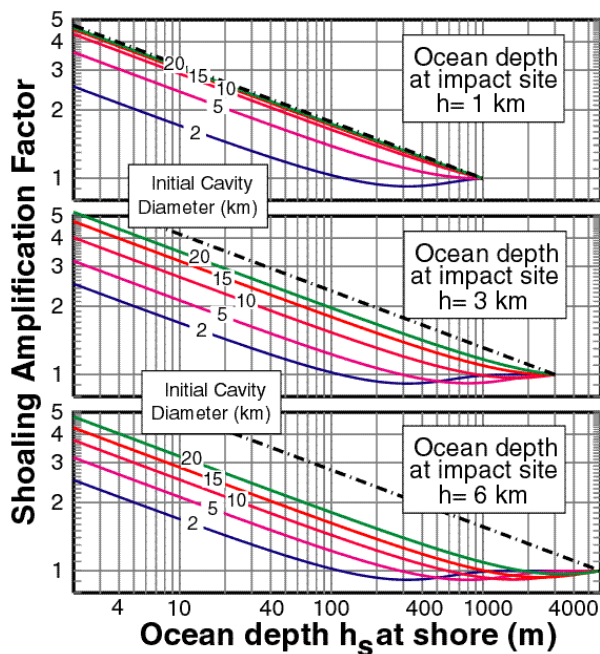


Figure 8. Tsunami shoaling factors from equation (19) for initial cavity diameters of 2, 5, 10, 15 and 20 km, and ocean depths at impact of 1, 3 and 6 km. The linear run-up factor is fairly constant between 2 and 5 over a wide range of conditions. The broken line is Green's Law, the $(h/h_s)^{1/4}$ shoaling factor appropriate for long waves. We do not attempt to model nonlinear components of run-up.

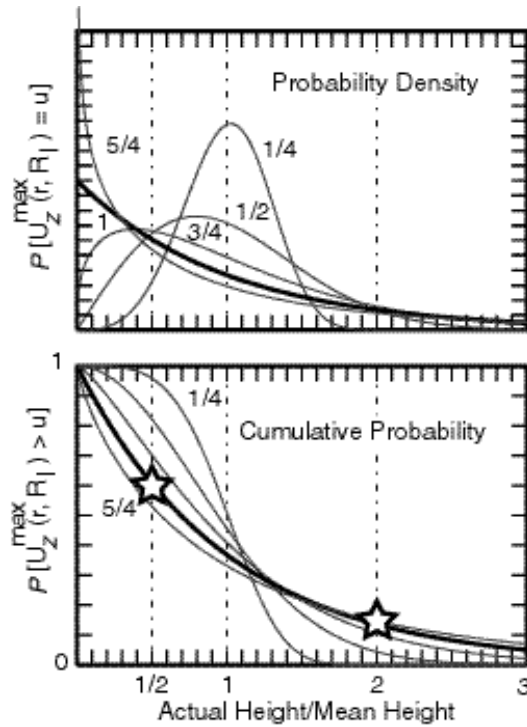


Figure 9. (top) Weibull likelihood distribution (equation 24) of actual tsunami height divided by mean height plotted for spread values $\alpha=1/4$ to $5/4$. (bottom) Probability that a tsunami will exceed some multiple of its mean height. The darkest curve is the case $\alpha=1$, close to the spread value assumed in these calculations.

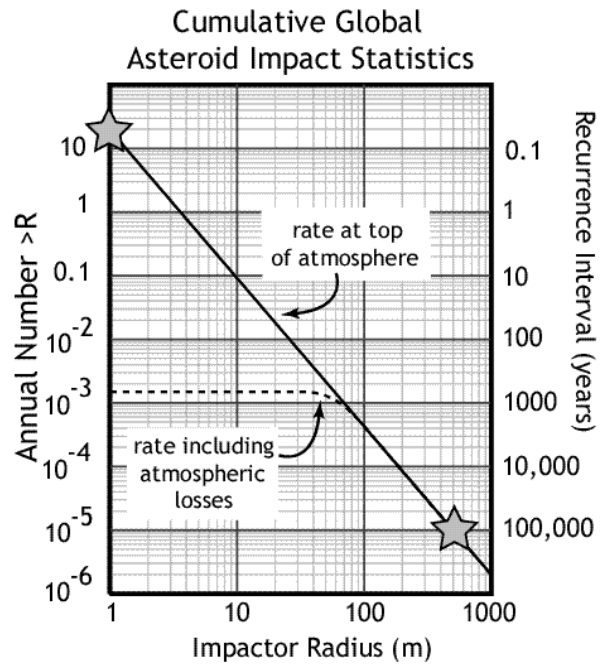


Figure 10. Cumulative bolide flux as a function of radius from equation (28) with constants a and b selected such that the line runs through the *Nemtchinov et al.* (1997) flux rate at small impactor radius (left star) and *Shoemaker et al.*'s (1990) rate at large radius (right star). The dashed line indicates the flux after correction for atmospheric losses.

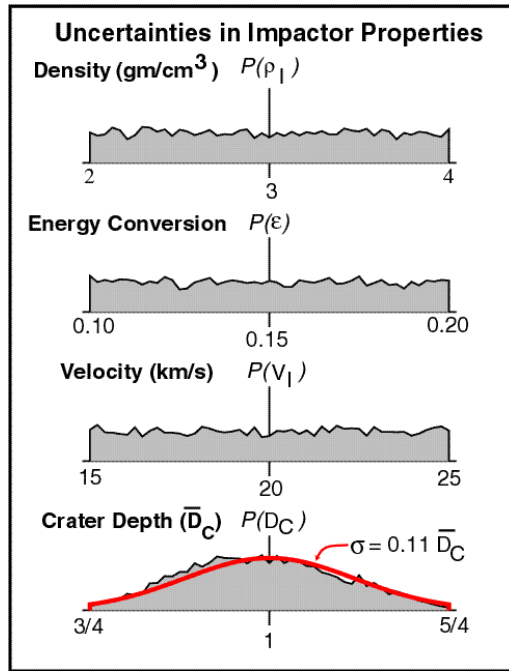


Figure 11. Effects of uncertainty of impactor properties on cavity depth. Each of impactor density, impactor velocity and energy conversion factor are modeled as having a uniform probability of occurrence within the stated limits. Values selected randomly and independently from these distributions produce a probability distribution of cavity depth (jagged shape, bottom panel). The smooth curve is a Gaussian function of mean D_c and standard deviation $0.11 D_c$ that fits the shape.

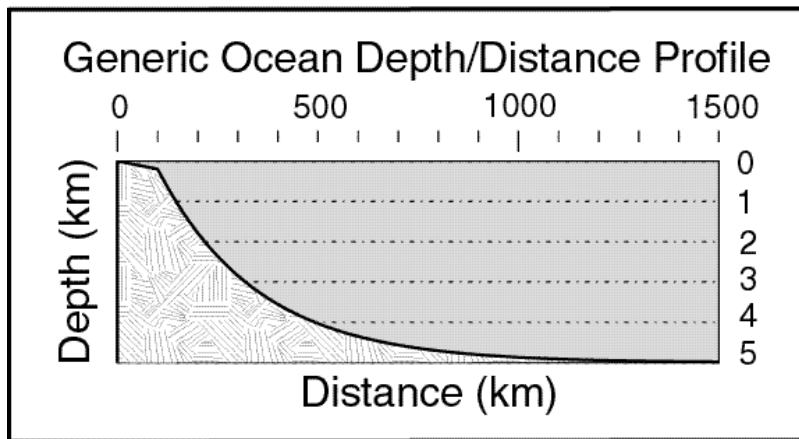


Figure 12. Ocean depth/distance profile used in the computation of site-generic tsunami hazard.

Hazard Breakdown by Impactor Size

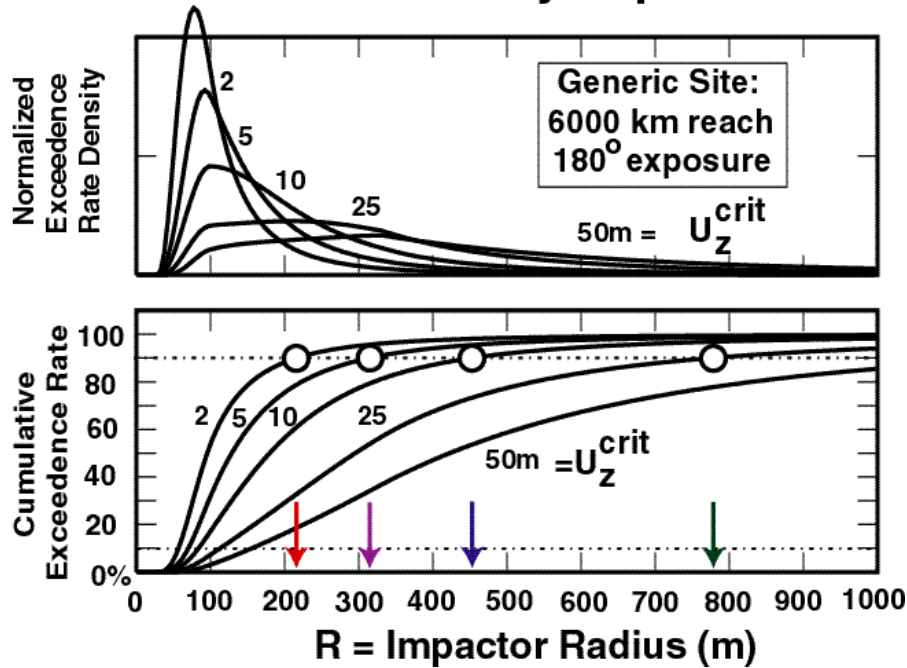
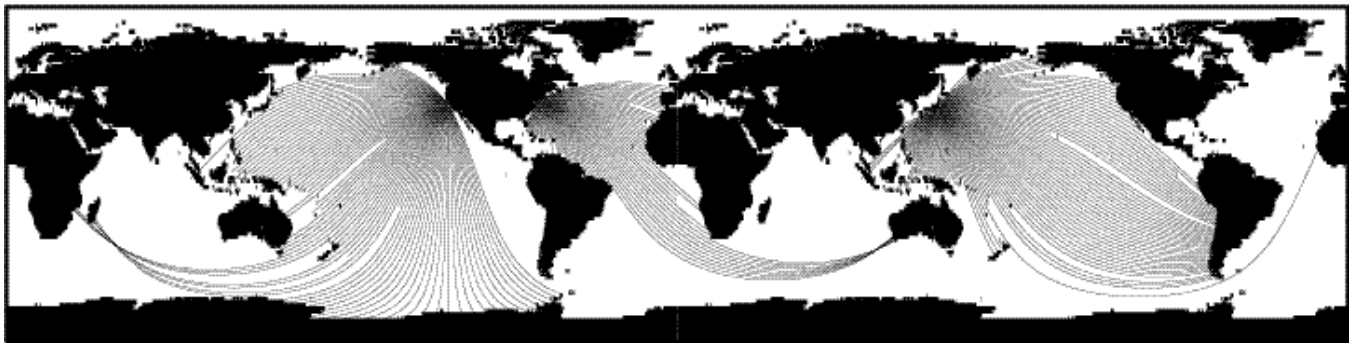


Figure 13. Breakdown of impact tsunami hazard (including atmospheric flux losses) versus impactor radius. The top panel shows normalized exceedence rate density at a generic coast site for tsunami height thresholds of 2, 5, 10, 25 and 50 m. The bottom panel graphs cumulative exceedence rate (in percent) versus impactor radius. The dots/arrows mark the radius at which 90% of total hazard is reached. For instance, 90% of 5 m tsunami come from impactors of 315 m radius or less

Site-Specific Tsunami Hazard

San Francisco New York Tokyo



Hilo

Perth Sydney

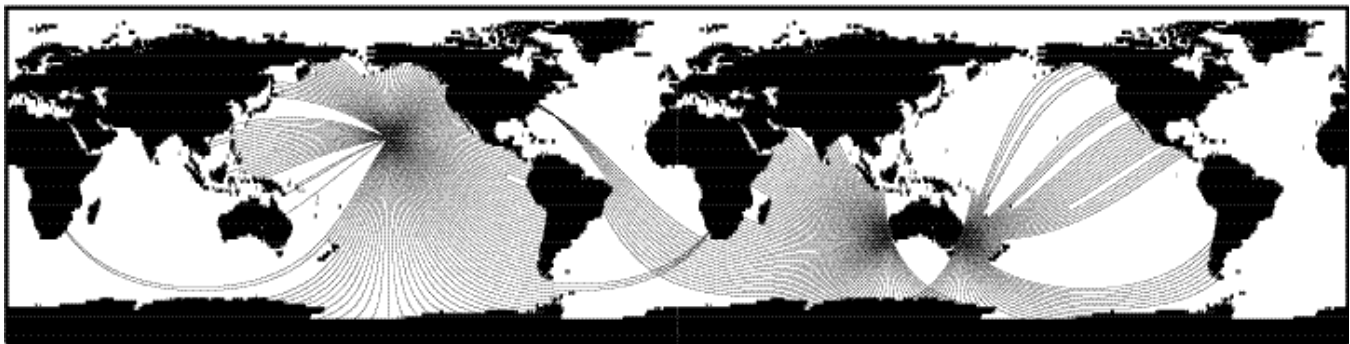
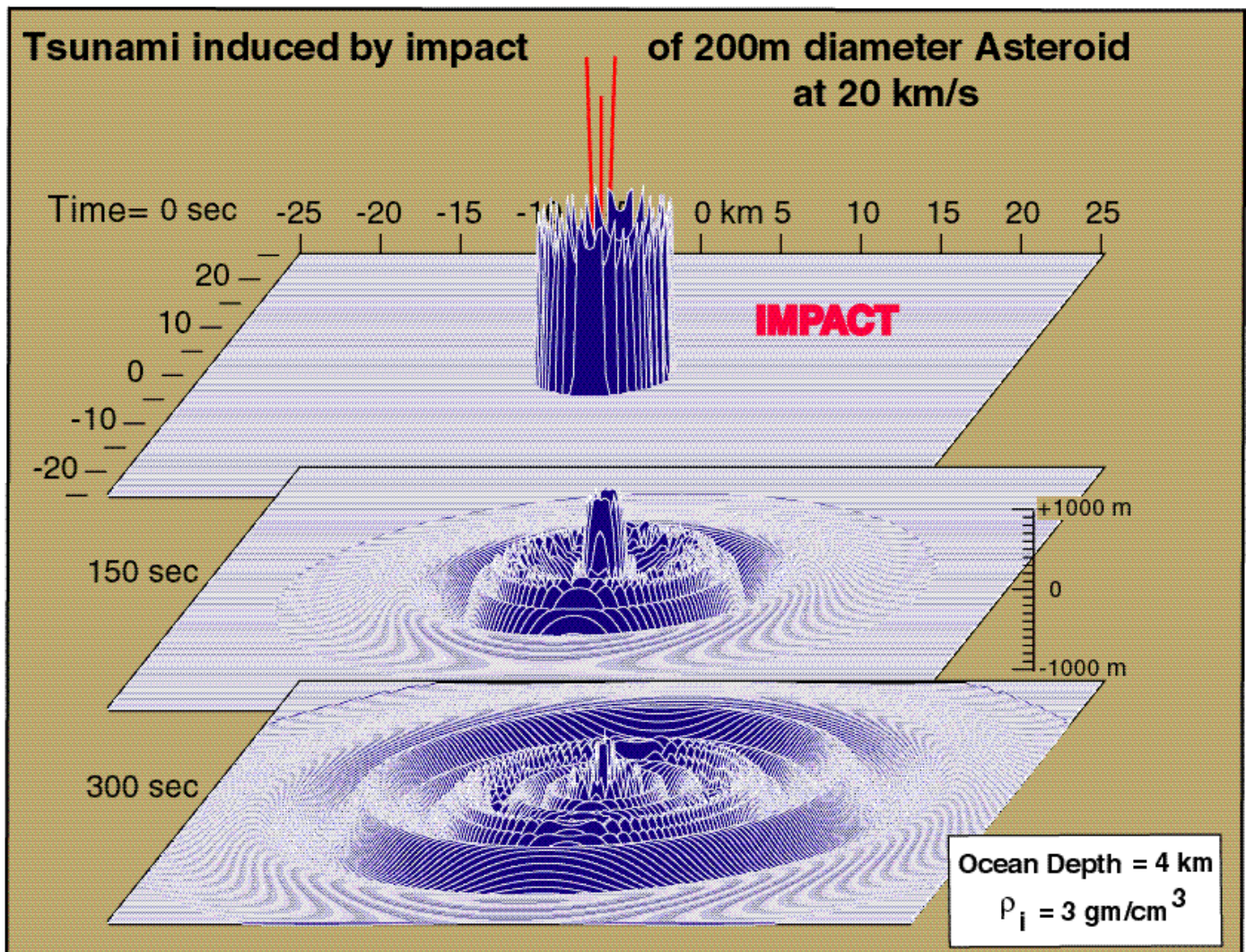


Figure 14. Tsunami source areas for site-specific hazard. The shaded areas are ocean regions over which equation (21) is integrated to get impact tsunami hazard for San Francisco, New York, Tokyo, Hilo, Perth and Sydney. Clearly, certain sites have a larger exposure to tsunami than others.



Cover Figure. Tsunami created by the impact of a 200 m diameter asteroid at 20 km/s. Within 300 seconds, tsunami rings expand to cover a 50x50 km section of the sea. Note that the tsunami separates into a great sequence of waves very soon after impact. The leading wave in the bottom panel is about 325 meters high.